Optical spectroscopy of high-*L* *n*=10 Rydberg states of nitrogen

P. L. Jacobson, R. D. Labelle, W. G. Sturrus,* R. F. Ward, Jr.,† and S. R. Lundeen

Department of Physics, Colorado State University, Fort Collins, Colorado 80523

(Received 22 November 1995)

A Doppler-tuned CO_2 laser was used to excite $n=10$ to $n=27$ Rydberg-Rydberg transitions in a fast beam of atomic nitrogen. The fine structure of $n=10$, $L=3-8$ Rydberg levels is partially resolved in the spectrum, giving experimental information about nitrogen Rydberg levels with $L>4$. The observed fine structure is well described by an effective potential whose empirical coefficients are adjusted to fit the data, giving estimates of the quadrupole moment and dipole polarizabilities of N^+. For the highest-L $n=27$ levels studied, the spectrum shows evidence of a transition to a new coupling regime where the N^+ hyperfine structure is larger than the Rydberg fine structure. [S1050-2947(96)01307-8]

PACS number(s): 32.30.Bv, 32.10.Dk, 32.10.Fn

I. INTRODUCTION

All atoms have many excited levels in which a single electron is excited to a level characterized by large values of orbital angular momentum, $L \geq 4$. In spite of this, relatively few of these high-L Rydberg levels have been resolved spectroscopically. In part, this is because the nonpenetrating high-L states have small quantum defects and can only be resolved in high-resolution spectroscopy. Also, however, selection rules prevent their observation in visible wavelengths with conventional absorption and emission spectroscopy. The few conventional spectroscopic observations are usually obtained with high-resolution far-infrared emission spectroscopy. In the case of atomic nitrogen, for example, the only published spectroscopic observation of excited levels with L of 4 or more is the study of $5G-4F$ emission lines near 4 μm [1].

In recent years, a new experimental technique has been developed which should allow observation of a wide variety of these high-L Rydberg levels. With this technique, the Rydberg states of interest are formed by charge exchange in a fast atomic beam and detected by resonant excitation with a Doppler-tuned CO_2 laser, followed by Stark ionization of the laser-excited atoms [2]. The frequency resolution of the laser excitation is sufficient to resolve the fine structure of individual high-L levels. Since selection rules allow all L levels to be excited, a wide variety of high-L levels can be spectroscopically resolved with this technique. The method was first applied in studies of helium [3], but has since been used to study molecular hydrogen [4,5], and atomic sulfur [6], neon [7], and carbon and oxygen [8]. In principle, it can be applied to any atom or molecule with a stable positive ion. The use of the CO_2 laser limits the technique to detection of levels with $n=9,10,11$, but it should be possible to extend this range with other lasers or slightly more complicated schemes. The range of L that can be resolved depends on the size of the fine structure. The typical experimental resolution of 0.005 cm^{-1} corresponds to a quantum defect of about

10^{-6} for $n=10$ Rydberg levels. In the study of atomic nitrogen reported here, this allows resolution of levels with L up to 8.

II. THEORY

The general structure of high-L atomic Rydberg levels is expected to be described by the ''jLK'' coupling scheme first discussed by Shortley and Fried [9] and by Racah [10] in connection with configurations such as p^5f. In such a configuration, the coupling between L_c and S_c in the open shell core is likely to be stronger than the electrostatic coupling between the core and the excited f electron, and this in turn is much stronger than the coupling to the excited electron's spin. Consequently, the good quantum numbers for such a configuration are expected to be

$$\vec{J}_c = \vec{L}_c + \vec{S}_c, \quad \vec{K} = \vec{J}_c + \vec{L}, \quad \vec{J} = \vec{K} + \vec{S}_R. \tag{1}$$

In the approximation in which the coupling to the excited electron spin is negligible, the pair of levels characterized by common J_c, L, and K, with

$$J = K \pm \tfrac{1}{2}$$

are degenerate. Because of this, the jLK coupling scheme is often referred to as ''pair coupling,'' and the levels denoted by jLK only. As the angular momentum L of the excited electron increases, this scheme is expected to become even more exact [11].

The Rydberg states of nitrogen have the configuration $2p^2nL$, which is also expected to display the jLK or ''pair-coupling,'' as discussed for the case of $L=3$ by Eriksson [12], and more generally by Gronlund [13]. The ground state of the N^+ ion is a ^3P level, with $J_c=0$, 1, or 2. Each of these core levels may bind a Rydberg electron and lead to an entire manifold of Rydberg levels, as illustrated in Fig. 1. In general, these will be characterized by J_c, n, L, and K, and we denote them here by

$$(J_c)nL_K.$$

As an example, Fig. 1 shows the levels with $n=10$ and $L=4-7$, bound to each core state. There are $2J_c+1$ possible
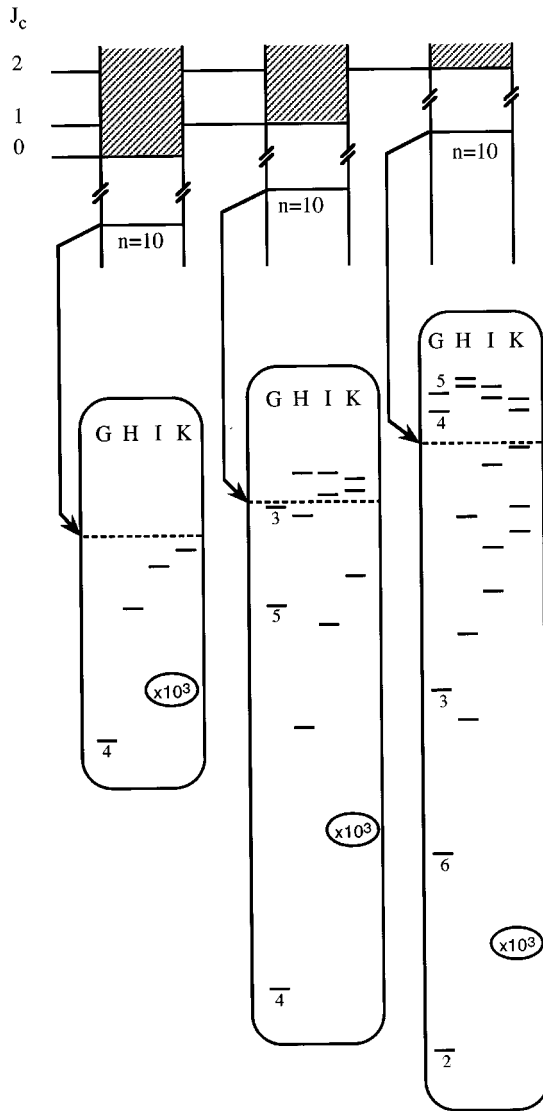
FIG. 1. Illustration of the pattern of high-*L* Rydberg fine structure in atomic nitrogen. Each fine-structure level of the N^+ core ($J_c = 0,1,2$) binds an entire series of Rydberg levels. The fine structure of $n = 10$ levels is shown in expanded scale to illustrate the typical pattern. In the case of the *G* levels, the numerals show the values of $K = J_c + L$ for each level. The scale of the figure is established by the core excitation energies, 48.7 cm^{-1} for $J_c = 1$ and 130.8 cm^{-1} for $J_c = 2$.

values of *K* in each case, with the differences in binding energy of these levels determined mostly by the quadrupole electrostatic interaction between the Rydberg electron and the ion core. Possible structure due to the Rydberg electron spin is neglected in Fig. 1.

A more detailed description of the Rydberg binding energies, which goes beyond the simple first-order perturbation theory of the central field approximation of Refs. [9,10,12, 13 expresses the nonhydrogenic interactions between the Rydberg electron and the positive-ion core in terms of an effective potential, V_{eff}. Defined within the subspace of Rydberg states of the system, i.e., those states where the ion core is in its ground state, this effective potential contains the effects of the Coulomb interactions to all orders. In this approach, exchange effects are neglected, and the Rydberg electron is

treated as distinguishable from the electrons in the core ion. The first few terms of this effective potential are given by

$$V_{eff} = -\left[\frac{e^2\alpha_s}{2r^4} + \frac{\eta}{r^6}\right] - \left[\frac{eQ}{r^3} + \frac{e^2\alpha_T}{2r^4} + \frac{C_6}{r^6}\right] \frac{\mathbf{X}_c^2 \cdot C^2(\Omega_R)}{\begin{pmatrix} 2 & 2 & 2 \\ -2 & 0 & 2 \end{pmatrix}},$$

(2)

where *r* and Ω_R are the radial and angular coordinates of the Rydberg electron and $\mathbf{X}_c$ is a second-rank tensor operator in the space of the core whose reduced matrix elements are defined by

$$\langle J_c = 2 | |X_c^2| | J_c = 2\rangle \equiv 1,$$

$$\langle J_c = 1 | |X_c^2| | J_c = 1\rangle \equiv -\sqrt{\tfrac{3}{7}},$$

$$\langle J_c = 0 | |X_c^2| | J_c = 0\rangle \equiv 0,$$

$$\langle J_c = 2 | |X_c^2| | J_c = 1\rangle \equiv \sqrt{\tfrac{9}{7}},$$ (3)

$$\langle J_c = 2 | |X_c^2| | J_c = 0\rangle \equiv \sqrt{\tfrac{4}{7}},$$

$$\langle J_c = 1 | |X_c^2| | J_c = 0\rangle \equiv 0.$$

The portion of V_{eff} proportional to *Q*, the electric quadrupole moment of the $J_c = 2$ state of the core, results from application of the Coulomb perturbation in first order. The matrix elements of X_c in other core states are computed on the assumption of pure *LS* coupling in the core. The portion of V_{eff} proportional to α_s and α_T, the scalar and tensor adiabatic dipole polarizabilities of the core, results from the lowest-order multipole terms of the Coulomb perturbation applied in second order. The coefficients η and C_6 combine higher-order and nonadiabatic effects. Both the diagonal and off-diagonal matrix elements of V_{eff} within the space of Rydberg states contribute to the Rydberg fine structure, according to

$$E[(J_c)nL_K] = \left(E_{core}(J_c) - \frac{\mathcal{R}}{n^2}\right) + \langle \Psi_0 | V_{eff} | \Psi_0 \rangle$$

$$+ \sum \frac{|\langle \Psi_0 | V_{eff} | \Psi'\rangle|^2}{E_0 - E} + \cdots .$$

$$\equiv E^{[0]} + E^{[1]} + E^{[2]} \qquad (4)$$

The result is in the form of a perturbation series in V_{eff}. The first bracketed term represents the zeroth-order energy, $E^{[0]}$, the next term, $E^{[1]}$, is the expectation value of V_{eff} in the *jLK*-coupled states, and the last term, $E^{[2]}$, in which the sum is over all other Rydberg states, describes mixing between different Rydberg series. If the Rydberg fine structure is small compared to the core fine-structure splittings and there is no coincidental degeneracy between Rydberg levels bound to different cores, then the contribution of $E^{[2]}$ is small. For example, in the case of the $n = 10$ nitrogen levels studied here, these terms have been calculated and found to be less than 0.01 cm^{-1} for all the $n = 10$ levels studied here and, therefore, only marginally significant at the precision of the present measurement. Both $E^{[0]}$ and $E^{[1]}$ are relatively simple to calculate:
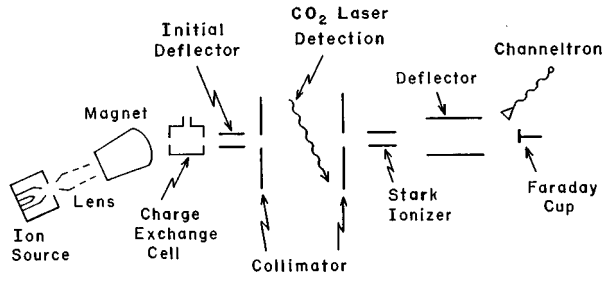
FIG. 2. A schematic diagram of the apparatus. The mass analyzed N^+ ion beam is neutralized in a charge-exchange cell to form a fast neutral beam containing N Rydberg states. The electric field in the initial deflector region ionizes any Rydberg levels with $n > 16$ and deflects ions out of the beam. The Doppler-tuned CO_2 laser excites Rydberg atoms from $n = 10$ to $n = 27$. Any excited atoms are ionized in the Stark ionizer and the resulting ions are deflected into a channeltron detector. The measured signal is the component of the channeltron current synchronous with modulation of the CO_2 laser amplitude. The Faraday cup monitors the total neutral beam by secondary emission, and can be used to compensate for fluctuations in the beam intensity.

$$E^{[0]} = E^0_{core}(J_c) - \frac{109\ 733.02\ \ cm^{-1}}{n^2},$$

$$E^{[1]} = A_0(nL) + A_2(nL)T(J_c, L, K),$$

where

$$T(J_c, L, K) = (-1)^{J_c + K} \langle J_c | |X_c^2| |J_c\rangle (2L+1)$$

$$\times \frac{\begin{pmatrix} L & 2 & L \\ 0 & 0 & 0 \end{pmatrix}}{\begin{pmatrix} 2 & 2 & 2 \\ -2 & 0 & 2 \end{pmatrix}} \begin{Bmatrix} K & L & J_c \\ 2 & J_c & L \end{Bmatrix}$$

and

$$A_0(nL) = -\frac{e^2 \alpha_s}{2} \langle r^{-4}\rangle_{nL} - \eta \langle r^{-6}\rangle_{nL},$$

$$A_2(nL) = -eQ\langle r^{-3}\rangle_{nL} - \frac{e^2 \alpha_T}{2}\langle r^{-4}\rangle_{nL} - C_6 \langle r^{-6}\rangle_{nL}, \tag{5}$$

where $\langle r^{-S}\rangle_{nL}$ are the hydrogenic radial expectation values for the nL electron [14]. Since these are decreasing functions of L, the pattern of high-L fine structure converges towards the hydrogenic limit as L increases. Figure 1 illustrates this fine-structure pattern for $n = 10$, $L = 4$–7 levels of nitrogen.

III. EXPERIMENT

The apparatus used for this study, shown schematically in Fig. 2, is similar to those used in previous studies with this technique [3–7]. A duoplasmatron ion source produces a 11-keV beam of N^+, which is mass analyzed and focused into a charge-exchange cell containing a few millitorr of atmosphere, where it is partially neutralized to form a fast atomic beam of nitrogen. In general, almost all possible excited states of N are formed at some level in this process. Only the small fraction formed in $n = 10$ levels is useful for this study. Immediately after the charge-exchange cell, the unneutralized ion beam is deflected away by an electric field that also serves the purpose of Stark ionizing and deflecting out of the beam any excited levels with $n > 16$. In the absence of laser excitation, the subsequent Stark ionization field, which is set at a slightly lower electric field, results in little or no additional ionization of the beam. As the neutral N beam passes through the CO_2 laser, however, atoms in $n = 10$ fine-structure levels may be excited to higher n levels *if* the Doppler-tuned laser frequency is resonant with an allowed transition. Coarse tuning of the laser is achieved by selecting one of the discrete CO_2 lines, $P(16)$ at 947.7 420, cm^{-1} for the $n = 10$–27 transitions. Fine tuning is then obtained by varying the angle of intersection between the laser and the fast atomic beam. The geometry of the Doppler-tuning stage is described in detail elsewhere [5]. For the nitrogen atomic beam velocity of $v/c = 0.001\ 306(1)$, this gives a continuous tuning range of about 1 cm^{-1}, comparable to the expected size of the $n = 10$ Rydberg fine structure. The apparent laser frequency seen by the moving atoms is given by

$$\nu' = \gamma \nu_L[1 + \beta \cos(\theta)], \quad \beta = \frac{v}{c}, \quad \gamma = (1 - \beta^2)^{-1/2}, \tag{6}$$

where ν_L is the laser frequency and Θ is the laser–atomic-beam intersection angle, measured from antiparallel. The resolution of the laser excitation is jointly determined by the transit time through the laser beam and the angular width of the fast beam. For the conditions of this experiment, the laser linewidth is approximately 0.005 cm^{-1}. As the laser angle is varied, individual $n = 10$ Rydberg levels will come into resonance for excitation to $n = 27$. Any excited atoms will be ionized by the Stark ionizing field and deflected into a channeltron electron multiplier. The measured signal is the component of the channeltron current synchronous with the chopping of the CO_2 laser.

Figure 3(a) shows typical signal data representing $n = 10$–27 transitions. For these data, the intersection angle was varied between 85° and 148° and is converted to energy according to Eq. (6). A rather complex spectrum of transitions is observed, spread out over about 1 cm^{-1}, with more than 30 separate transitions resolved. All of these are close to the hydrogenic $n = 10$–27 transition frequency, 946.8048 cm^{-1}. Since the electric dipole selection rules for the transition require $\Delta J_c = 0$, excitation transitions in all three Rydberg systems illustrated in Fig. 1 ($J_c = 0,1,2$) are all expected to occur at approximately this frequency. Since the fine structure of $n = 27$ levels is substantially smaller than that of the $n = 10$ levels, the observed spectrum is approximately a map of the $n = 10$ fine structure, with more tightly bound levels occurring at higher excitation frequencies.

The limiting factor in the precision of this Doppler-tuned spectroscopy is knowledge of the intersection angle Θ in Eq. (6). This angle is varied using the rotation stage described in Ref. [5]. With this device, the laser beam enters the vacuum system aligned along the rotation axis of a turntable carrying fixed mirrors that redirect the beam across the rotation axis at the height of the atomic beam. The intersection angle varies
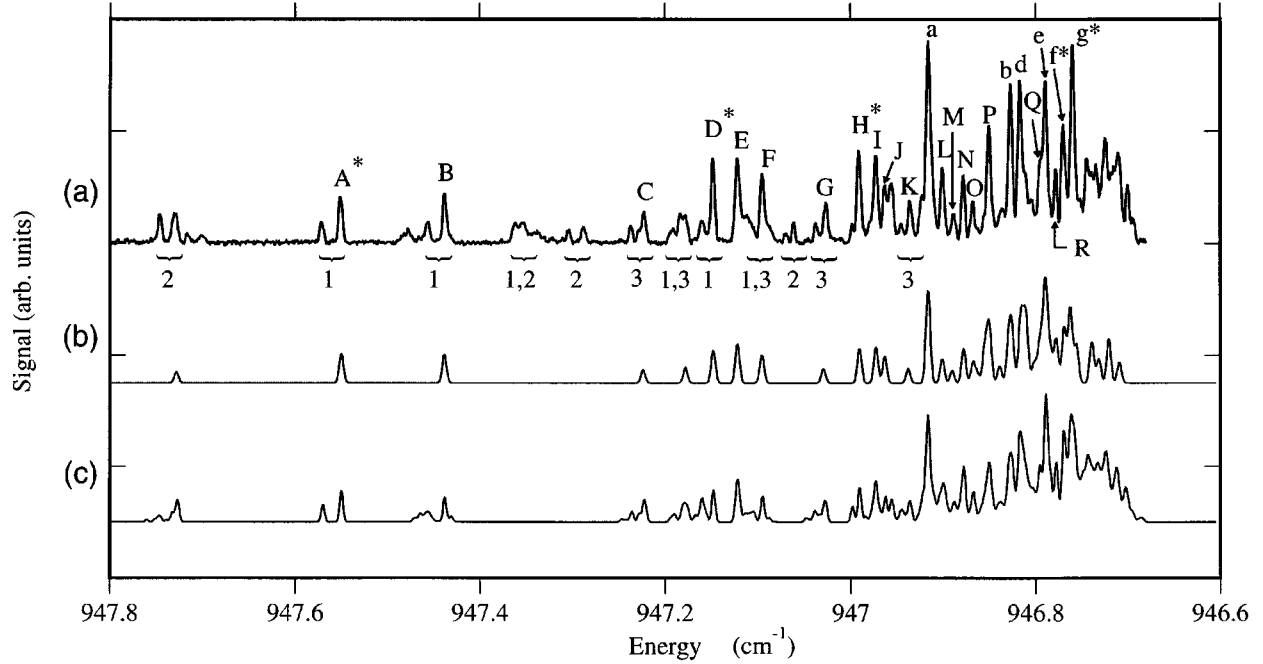
FIG. 3. (a) Experimental spectrum of $n=10-27$ transitions in atomic nitrogen. Approximately 40 separate lines are well resolved, due to the fine structure of the $n=10$ Rydberg levels. The primary unblended lines are identified with capital letters $A-R$. A number of blended lines are identified with lower case letters $a-g$. The characteristics of these lines are discussed in the text. The notations, 1,2,3, below the lines indicate spectral features that are discussed in the text.   (b) Theoretical simulation of the primary spectral lines using equations in the text to model the line positions and strengths, and including $n=10$, $L=4-9$ levels.   (c) Improved theoretical simulation, including transitions to all possible $n=27$ levels, and including the effects of $n=27$ hyperfine structure. The relative strength of transitions sharing the same initial level is assumed to be proportional to the square root of the rms z matrix element, as discussed in the text.

as the turntable rotates under the control of a precision rotation stage (Newport 496) controlled electronically (Newport PMC100). There are two problems with this arrangement. First, the stage angle that corresponds to $\Theta=0$, i.e., to counterpropagating laser and atomic beam, is difficult to determine directly. While this absolute angle can be set to within a degree or so by rotating the stage until the laser beam propagates directly downstream, in practice there is a small unknown offset angle between true $\Theta=0$ and a stage angle reading of zero. Second, if the CO_2 laser is not aligned precisely along the stage rotation axis, then as the stage rotates, the laser beam will ''walk'' on the stage mirrors, resulting in small additional changes in the intersection angle. Previous studies [5], have indicated that these lead to sinusoidal errors in the intersection angle. Thus, in general, the relationship between the angle measured electronically for the rotation stage Θ_{obs} and the actual intersection angle Θ is given by

$$\theta = \theta_{obs} + A + B \cos(\theta_{obs}) + C \sin(\theta_{obs}). \quad (7)$$

The calibration constants A, B, and C were determined by observing the $n=10-27$ transition in atomic hydrogen with four different CO_2 lines, for which the transition occurred at widely varying angles. Knowing the actual transition frequency, 946.3265 cm^{-1} and the angles Θ_{obs} at which the transition is observed for each laser line, Eq. (7) can be substituted into Eq. (6) and the result fitted to determine the constants A, B, and C, along with the hydrogen beam velocity. Table I shows one example of such a fit and the constants derived from it. Clearly, the major effect is the offset angle A, about 1° for these data, and the alignment errors B and C

are much smaller. When Eq. (6) is used for nitrogen spectra, of course, the smaller velocity

$$\frac{V_{N^+}}{V_{H^+}} = \left[\frac{M_{H^+}}{M_{N^+}}\right]^{1/2} = \frac{1}{\sqrt{13.9014}},$$

TABLE I. Typical observations of the $n=10-27$ transition in atomic hydrogen, used to calibrate the Doppler-tuning angle. Four different CO_2 lines, whose frequencies are shown in column 2, were used to excite this transition ($\nu_0 = 946.3265$ cm^{-1}) at eight different settings of the rotation stage, Θ_{obs}. These eight observations were fit using Eqs. (6) and (7) of the text to determine the calibration constants A, B, and C and the proton velocity β shown at the bottom of the table. The fitted angles Θ_{fit} and their deviations from the observations are shown in columns 4 and 5.

CO_2 line	ν_1 (cm^{-1})	$\Theta_{obs.}$ (deg)	Θ_{fit} (deg)	$\Theta_{obs} - \Theta_{fit}$ (deg)
$P(14)$	949.4793	−134.09	−134.08	−0.01
$P(16)$	947.7420	−108.77	−108.77	+0.00
$P(18)$	945.9802	−86.52	−86.54	+0.02
$P(20)$	944.1940	−63.28	−63.26	−0.02
$P(20)$	944.1940	60.87	60.89	−0.02
$P(18)$	945.9802	84.15	84.13	0.02
$P(16)$	947.7420	106.32	106.31	0.01
$P(14)$	949.4793	131.57	131.59	−0.02

Best-fit parameters:

$\beta = 0.004\ 868(1)$, $A = 1.211(8)°$, $B = -0.041(20)°$, $C = 0.497(9)°$

characterizing N^+ at the same accelerating potential used for H^+, was used [15], but the angle calibration constants A, B, and C were unchanged.

Because of variations in the alignment of the CO_2 laser, some day-to-day variation in the constants A, B, and C was observed. In order to achieve the highest precision possible in the determinations of the transition frequencies represented in Fig. 3(a), six strong lines, denoted there with asterisks, were chosen for more careful measurement. In two separate measurements, the angular positions of each of these six lines were carefully determined in a run preceded by and followed by a calibration run in which the angular positions of all eight hydrogen transitions of Table I were determined. The energies of the six transitions from each run were then determined by using both the ''pre'' and ''post'' calibration data, giving a total of four determinations of each transition energy. The maximum variation of any of these four determinations from the appropriate mean transition energy was 0.0012 cm^{-1}, and the mean-squared standard deviation of the transition measurements was 0.0005 cm^{-1}. We choose to assign an error of ± 0.001 cm^{-1} to the mean transition energy for each of these directly calibrated lines. This is approximately the expected limit of precision due to possible drift in the frequency of the unstabilized CO_2 laser. The laser has a cavity free spectral range of 100 MHz and a gain profile width of approximately 200 MHz, allowing an average frequency drift of about ± 20 MHz or 0.0007 cm^{-1}.

Comparison of the transition energies determined for the six lines discussed above with the transition energies for the same six lines determined from the line scan of Fig. 3(a), using calibration constants determined at the time of the scan showed agreement to within 0.003 cm^{-1} for all six of the lines. Small adjustments in the angular calibration constants A and B for the scan reduced the errors to less than 0.0005 cm^{-1} for all six lines. The same adjusted calibration constants were then used to determine the transition energies for all 24 of the labeled lines in Fig. 3(a). This procedure effectively uses the six directly calibrated lines as secondary calibration standards, thus indirectly calibrating the transition frequencies of the other 18 transitions in Fig. 3(a). Since the six directly calibrated lines cover the entire range of the spectrum, we assign the same ± 0.001 cm^{-1} error to the indirectly calibrated lines. The transition energies so determined are shown in Table II, along with the line strengths. The arbitrary alphabetical labels correspond to Fig. 3(a).

IV. DATA ANALYSIS

By comparing the observed spectrum of Fig. 3(a) with simulations based on previous estimates of the core parameters Q and α_S [1], a tentative identification of 18 unblended lines was made. The transition energies corresponding to these 18 lines, labeled $A-R$ in Fig. 3(a), are shown in Table II. They were used to obtain an improved estimate of the core parameters in V_{eff}, as illustrated in Table III. Starting with initial estimates of the core parameters in V_{eff} [1], each transition energy was used to infer $E^{[1]}$ for the $n=10$ level, using

$$E^{[1]}(10) = 946.8048 \ \text{cm}^{-1} - \Delta E_{\text{trans}} + E^{[1]}(27) - E^{[2]}(10),$$
(8)

TABLE II. Summary of line positions and strengths in the $n=10–27$ Rydberg transition spectrum of Fig. 3. Unblended lines are identified by their lower state. In all cases, the upper state is the $n=27$ level satisfying $\Delta J_c = 0$, $\Delta K = \Delta L = 1$. Asterisks identify directly calibrated lines, as discussed in the text.

Line	Energy (cm^{-1})	Strength	$n=10$ Level
A*	947.5507(10)	42.7	$(1)10G_4$
B	947.4376(10)	42.6	$(2)10G_6$
C	947.2225(10)	27.2	$(2)10H_3$
D*	947.1480(10)	71.9	$(1)10H_5$
E	947.1218(10)	73.4	$(0)10G_4$
F	947.0952(10)	51.9	$(2)10H_7$
G	947.0268(10)	36.1	$(2)10I_4$
H*	946.9908(10)	75.4	$(1)10I_6$
I*	946.9727(10)	61.3	$(1)10G_5$
J	946.9630(10)	50.6	$(2)10I_8$
K	946.9356(10)	31.2	$(2)10K_5$
L	946.9007(10)	58.7	$(2)10K_9$
M	946.8885(10)	23.5	$(2)10L_6$
N	946.8780(10)	56.3	$(1)10L_8$
O	946.8677(10)	28.4	$(2)10L_{10}$
P	946.8503(10)	87.4	$(0)10I_6$
Q	946.7951(10)	74.4	$(1)10I_7$
R	946.7783(10)	60.0	$(1)10L_7$
a	946.9159(10)	167.1	blended
b	946.8271(10)	124.3	blended
d	946.8169(10)	129.6	blended
e	946.7894(10)	122.0	blended
f*	946.7704(10)	95.5	blended
g*	946.7598(10)	149.0	blended

where ΔE_{trans} is the observed transition energy and $E^{[1]}(27)$ and $E^{[2]}(10)$ are small corrections calculated with the initial estimates of the core parameters. This expression is obtained from Eq. (4) after noting that $E^{[2]}(27)$ is negligibly small. The resulting values of the $n=10$ first-order energies can be fit to Eq. (5) to determine new estimates of the core parameters. These can then be used to recalculate the terms $E^{[1]}(27)$ and $E^{[2]}(10)$, which occur on the right-hand side of Eq. (8), and the process repeated until a stable solution is found. Because these terms are very small, as illustrated in Table III, the convergence of this process is rapid. The final results of such a fit are shown in Table III. The new core parameters found are

$$Q = -0.364(6)ea_0^2,$$

$$\alpha_s = 3.77(11)a_0^3,$$

$$\alpha_T = 0.3(4)a_0^3,$$

$$\eta = -8(5)e^2a_0^5,$$

$$C_6 = -10(16)e^2a_0^5.$$

The uncertainties assigned to these estimates were determined after allowance for possible correlation in the errors from the various measured line positions.

TABLE III. Details of the fit used to determine the best values of the N^+ core parameters by comparison with the $n=10$ Rydberg level structure. Column 1 identifies the line, for reference to Table I. Columns 2, 3, and 4 tabulate small corrections used in computing the $n=10$ fine-structure energies, $E^{[1]}(10)$, which were fit to determine the core parameters. This computation used Eq. (8) of the text, except that some of the transition energies ΔE were corrected to compensate for the very slight line shifts caused by $n=27$ hyperfine structure. Column 4 shows this small correction, $\delta E_{\text{HFS}}(27)$. The resulting values of $E^{[1]}(10)$ for each level are shown in column 5 and the fitted values found from Eq. (5) of the text are shown in column 6. The best-fit parameters are listed at the bottom of the table. Unless otherwise stated, all values are in cm^{-1}.

Transition	$E[1](27)$	$E[2](10)$	$\delta E_{\text{HFS}}(27)$	$E[1](10)$	E_{fit}
A	−0.0184	−0.0026	0.0000	−0.7617(10)	−0.7612
B	−0.0157	−0.0078	0.0003	−0.6409(10)	−0.6414
C	−0.0120	0.0015	0.0014	−0.4326(10)	−0.4324
D	−0.0101	−0.0003	0.0000	−0.3530(10)	−0.3528
E	−0.0065	−0.0017	0.0000	−0.3217(10)	−0.3219
F	−0.0086	−0.0019	0.0005	−0.2976(10)	−0.2977
G	−0.0072	−0.0006	0.0015	−0.2302(10)	−0.2313
H	−0.0061	0.0000	0.0000	−0.1921(10)	−0.1918
I	−0.0019	−0.0073	0.0000	−0.1625(10)	−0.1622
J	−0.0053	−0.0006	0.0007	−0.1635(10)	−0.1628
K	−0.0046	0.0002	0.0016	−0.1373(10)	−0.1378
L	−0.0035	0.0002	0.0008	−0.0999(10)	−0.0994
M	−0.0032	0.0001	0.0017	−0.0886(10)	−0.0866
N	−0.0028	0.0000	0.0000	−0.0760(10)	−0.0757
O	−0.0024	0.0000	0.0010	−0.0663(10)	−0.0654
P	−0.0014	−0.0001	0.0000	−0.0467(10)	−0.0471
Q	0.0006	−0.0007	0.0000	+0.0111(10)	+0.0108
R	0.0010	−0.0001	0.0000	+0.0275(10)	+0.0281

Best-fit parameters:
$Q=-0.364(6)\ ea_0^2$, $\alpha_s=3.77(11)\ a_0^3$, $\alpha_T=0.3(4)\ a_0^3$, $\eta=-8(5)\ e^2a_0^5$, $C_6=-10(16)\ e^2a_0^5$

The values of Q and α_s determined in this way are somewhat different than the estimates of Ref. [1] ($Q=-0.366$, $\alpha_s=3.60$). The degree of agreement is in part fortuitous since our analysis takes into account the higher-order terms (α_T, η, and C_6) neglected in Ref. [1].

The pattern of line intensities shown in Table II indicates a slow decrease in intensity as either J_c or L increases. This pattern can be crudely parametrized by the expression

$$I=(2K_i+1)(10.02-1.94J_c-0.55L_i), \qquad (9)$$

where L_i and K_i are the quantum numbers of the initial $n=10$ level and the numerical coefficients are estimated from the intensities of the 18 lines labeled $A-R$ in Table II. For these 18 lines, the fitted values of the intensity from Eq. (9) match the observations to within about 15%. This is sufficiently precise to test the tentative line identifications by simulating a spectrum containing all lines originating in all the $n=10$ levels with $L=4-9$. Such a simulated spectrum is shown in Fig. 3(b). Only the strongest transitions, corresponding to the transitions

$$(J_c)10L_K \rightarrow (J_c)27(L+1)_{K+1}$$

are included in the simulation, with intensities as given by Eq. (9) and positions predicted by Eq. (5) using the parameters listed above. Most of the strongest features in the spectrum are well reproduced in the simulation. A number of the strongest lines in the spectrum are found to be blends of two

or more lines. These are identified with lower case letters, a,b,d,e,f,g in Fig. 3. Table IV shows the observed line positions and total strengths for these six blended lines, and compares them with the expected line position based on Eq.

TABLE IV. Tabulation of blended line compositions. Column 1 identifies the line from Fig. 3(a). The observed transition energies and line strengths have been given in Table II. Column 2 identifies the several transitions composing the blended line, listing the lower state. Columns 3 and 4 show the calculated line position and strength. The total strength is shown in Column 5.

Line	Lower state	Calculated ν	Strength	Total strength
a	$(1)10K_7$	946.9168	63.5	
	$(0)10H_5$	946.9161	80.0	
	$(2)10H_4$	946.9168	30.5	173.9
b	$(0)10K_7$	946.8258	92.6	
	$(1)10H_6$	946.8272	69.3	161.8
d	$(0)10L_8$	946.8152	95.5	
	$(1)10G_3$	946.8147	41.2	136.7
e	$(1)10K_8$	946.7883	71.9	
	$(1)10L_9$	946.7889	69.9	141.8
f	$(1)10K_6$	946.7697	55.0	
	$(2)10L_9$	946.7691	33.1	88.1
g	$(1)10H_4$	946.7617	48.0	
	$(1)10I_5$	946.7614	52.6	100.6

(5) and the simulated strength based on Eq. (9). The satisfactory agreement between the calculated strength and positions of the blended lines and the observations confirms the identifications of the 18 unblended lines.

V. ADDITIONAL DETAILS OF THE SPECTRA

Several features of the spectrum of Fig. 3(a) are not reproduced in the simulation of Fig. 3(b). We wish to understand the reason(s) for this in order to be sure that they do not call into question the conclusions drawn from the previous line identifications. For the most part, the simulation contains fewer lines than the data. There are several reasons for this.

(1) For each $n=10$ level, the simulation of Fig. 3(b) includes only the single transition to the upper state satisfying $\Delta K = \Delta L = 1$. While these transitions certainly have the largest dipole matrix elements, transitions to other upper states are not strictly forbidden in many cases. For example, the transition labeled A is from the $(1)10G_4$ to the upper state $(1)27H_5$. A weaker transition is allowed to the $(1)27H_4$ state, which, according to Eq. (5), lies about 0.020 cm^{-1} higher in energy. This is in good agreement with the position of the satellite transition labeled 1 just to the left of transition A in Fig. 3(a). However, since the rms z matrix element for the $\Delta K=0$ transition is $\frac{1}{9}$ of that for the $\Delta K=1$ transition, a naive estimate of relative transition strengths would suggest $\frac{1}{81}$, much smaller than shown in the spectrum. That this estimate is incorrect was shown clearly in a recent study of high-L states of sulfur [6], where similar weak transitions were observed. In that study, the transition strength was found to be controlled by the power broadening of the homogeneous laser line shape in the presence of the inhomogeneous width representing the Doppler width of the fast atomic beam. Calculations based on this model predict a line strength approximately proportional to the square root of the dipole matrix element, in good agreement with observations [6]. A similar dependence was deduced for the line strengths of the present experiment from the measured variation of the strengths of several lines with laser power. Applying this prediction to the satellite transition of line A in Fig. 3(a) leads to a predicted relative strength of $\frac{1}{3}$, in good agreement with the observations. Several other ''extra'' lines in the experimental spectrum can also be explained in this way. They are all labeled 1 in Fig. 3(a).

(2) Several of the ''extra'' lines in the experimental spectrum can be attributed to excitation of 10F Rydberg levels of nitrogen. For example, the pair of lines near 947.29 cm^{-1} can be attributed to the transition $(1)10F_2$ $(1)27G_3$ and the group of lines near 947.35 can be attributed to the transition $(2)10F_3-(2)27G_4$. Both of these are labeled by 2 in Fig. 3(a). An interesting feature of these lines originating from 10F levels is that they appear to be double, but with a doublet splitting that is not constant. We have investigated this further by studying a number of other 10F excitations not shown in Fig. 3(a). The results of these studies are summarized in Table V. Eight lines were observed, whose doublet splittings varied from 0.00 to 0.028 cm^{-1}. For example, the line at 947.29 in Fig. 3(a) shows one of the largest splittings, 0.016. We attribute these splittings to the previously neglected difference in energy between the $J=K\pm\frac{1}{2}$ Rydberg

TABLE V. Summary of positions and exchange energy splittings of observed 10F levels of nitrogen. Column 1 identifies the F level. Column 2 shows the difference of the observed $n=10$–27 or $n=10$–29 excitation energy from the hydrogenic transition energy. Column 3 shows the predicted transition energy, in the same terms, using Eq. (5) of the text. These predictions appear consistently too small by approximately 0.1 cm^{-1}. Column 4 shows the observed exchange energy splitting, and column 5 shows the calculated splittings, adjusted to agree in the case of the first listed line. All values are in cm^{-1}.

F state	Δ_{obs}	Δ_{calc}	δE_{obs}	δE_{calc}
$(2)10F_5$	1.88	1.79	0.028	0.028
$(2)10F_4$	0.26	0.10	0.010	0.020
$(2)10F_3$	0.55	0.32	0.000	0.001
$(2)10F_2$	1.56	1.49	0.009	0.010
$(2)10F_1$	2.76	2.72	0.010	0.008
$(1)10F_4$	0.93	0.79	0.016	0.014
$(1)10F_3$	2.17	2.13	0.012	0.016
$(1)10F_2$	0.49	0.31	0.016	0.016
$(0)10F_3$	1.19	1.11	0.007	0.010

states of the same J_c, L, and K. According to the calculation of Gronlund [13], these splittings would be expected to be dominated by the exchange integral, $G^2(2p,10f)$, and should therefore occur in a pattern that is determined up to a constant by Gronlund's calculation. As Table V illustrates, the observed splittings are in satisfactory agreement with this predicted pattern. We choose not to use these 10F lines in determining the N$^+$ core parameters since the effective potential theory may not apply as well to these relatively low-L levels. However, the small size of the observed F-state exchange energies supports our assumption that the exchange energies, which are expected to decrease rapidly with L, are negligible for the higher-L levels.

(3) Finally, a number of lines in the experimental spectrum of Fig. 3(a) show ''satellite'' features that are related to the hyperfine structure of N$^+$. These are labeled 3 in Fig. 3(a). The transition C, for example, is from the $(2)10H_3$ level to the $(2)27I_4$ level. Since there is no $(2)27I_3$ level, there is no possibility of a compound line shape due to a $\Delta K=0$ transition for this line, but nevertheless, a compound structure is observed. In order to understand this structure, it is necessary to consider the effects of hyperfine interactions on the Rydberg structure, which has so far been neglected. For simplicity, we consider only the dipole hyperfine structure

$$H_{\text{HFS}}=A_{\text{HFS}}(\vec{J}_c\cdot\vec{I}), \qquad (10)$$

where I is the nuclear spin, equal to 1 for ^{14}N, and the coefficient A_{HFS} has been measured to be 0.003 15 cm^{-1} for the $J_c=2$ ground state of N$^+$ [16]. In the free N$^+$ ion, this interaction splits the $J_c=2$ level into three levels with $F=J_c+I$ equal to 3, 2, or 1, spanning an energy range of 0.016 cm^{-1}. In the $n=10$, $L=4$–8 Rydberg levels of N studied here, the fine-structure interactions represented by Eq. (2) couple J_c more strongly to L, the Rydberg angular momentum, than is coupled to I by Eq. (10). Consequently, the hyperfine eigenstates of the Rydberg levels are given approximately by the coupling scheme:
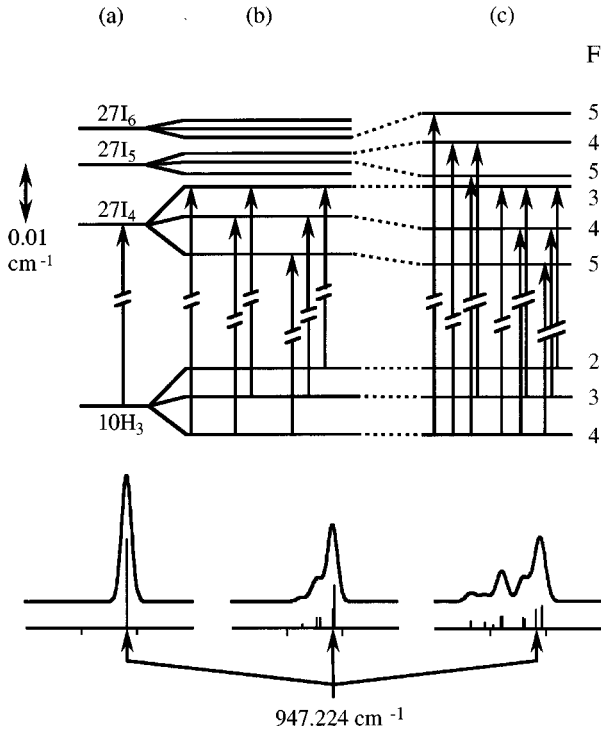
FIG. 4. Illustration of the effects of hyperfine structure on the $(2)10H_3$-$(2)27I_4$ transition, labeled C in Fig. 3(a). (a) Neglecting hyperfine structure, only a single transition is possible. The stick diagram below shows the simulated line shape. (b) Including the hyperfine structure in the approximation of Eq. (12) of the text, both upper and lower states are split into three levels with comparable splittings. The primary resonance transitions are shifted very little from case (a). Additional weak resonance components appear, distorting the simulated line shape slightly, as shown in the simulation below. (c) The actual hyperfine structure is obtained by diagonalizing the full Hamiltonian, including both fine and hyperfine structure. This mixes fine-structure levels of different K, and results in additional allowed transitions to the higher energy portion of the $(2)10H$ manifold. The simulated spectrum, shown below, is in very good agreement with the experimental observations in Fig. 3(a).

$$\vec{K}=\vec{J}_c+\vec{L}, \quad \vec{F}=\vec{K}+\vec{I}. \quad (11)$$

In states of this type, when the hyperfine structure is small compared to the fine structure, it is given by

$$\Delta E_{\text{HFS}}=A_{\text{HFS}}\left[\frac{K(K+1)+J_c(J_c+1)-L(L+1)}{2K(K+1)}\right](\vec{K}\cdot\vec{I}). \quad (12)$$

For example, the $(2)10H_3$ state is split into three levels with $F=4$, 3, and 2, spanning an energy range of 0.011 cm^{-1}. Since the scale of this structure is comparable to the resolution of the optical spectroscopy of Fig. 3, it may at first seem surprising that the effects of hyperfine structure are not more immediately apparent in the spectra. The reason for this is that, as long as the upper state of the optical transition is also described by this coupling scheme, its hyperfine structure is similar in scale to the lower level *and* transition selection rules restrict the possible transitions in such a way that the net contribution of hyperfine structure to the position of the

transition resonance is very small. For example, Fig. 4(a) illustrates the $(2)10H_3$ and $(2)27I_4$ levels of N in the absence of hyperfine structure. Transitions between these two levels lead to transition C in Fig. 3(a). Figure 4(b) illustrates the hyperfine structure of the these two levels, calculated in the approximation of Eq. (12). The stick diagrams and simulated line shapes shown below Figs. 4(a) and 4(b) illustrate the expected compound line shape observed in each case. The relative line strengths in the compound line are determined from the square root of the rms z matrix element. Clearly, the effects of hyperfine structure on the line shape are quite minor if the approximation of Eq. (12) is valid.

If, however, the size of the upper state fine structure is comparable or less than the core hyperfine splittings, then the upper state is no longer described by the coupling scheme of Eq. (11), and Eq. (12) is invalid. In this case, the eigenstates are found by diagonalizing the Hamiltonian, which is the sum of Eqs. (2) and (10), and they are in general no longer eigenstates of K. This is, of course, the actual case for the $(2)27I$ states of N, as illustrated in Fig. 4, and the resulting eigenvalues, for the levels contributing to the transition from the $(2)10H_3$ level, are illustrated in Fig. 4(c). This mixing of states of different K states by the hyperfine interaction distributes the transition strength from a particular lower state more broadly through the complex manifold of $n=27$ levels. As a result, transitions terminating on an upper level in this intermediate coupling regime can assume a much more complex structure, such as that illustrated for the $(2)10H_3$–$(2)27I_4$ transition in Fig. 4(c). The predicted compound line shape closely matches the observed experimental line shape for this transition shown in Fig. 3(a). A match of similar quality is also obtained in simulations of transitions F, G, and K in Fig. 3(a). The simulations also show a small downward shift (<0.002 cm^{-1}) of the primary resonance component from the position expected in the absence of hyperfine structure. Since these shifts are larger than the uncertainties in the line positions, they were applied as corrections in Table III, where they are denoted $\delta E_{\text{HFS}}(27)$, before the line positions were used to estimate core parameters.

Since the hyperfine structure of the $J_c=1$ state is expected to be much smaller than that of the $J_c=2$ state [16], and the $J_c=0$ state has no hyperfine structure, only lines involving $J_c=2$ Rydberg levels are subject to this complicating factor.

Figure 3(c) shows a simulation of the excitation spectrum of $n=10$ $L=4$–9 states of N including the effects (1) and (3) discussed above. For this simulation, the relative strength of lines originating from a common $n=10$ level was approximated as the square root of the rms z matrix element for the transition, and the relative strength of lines from different $n=10$ levels was assigned from Eq. (9), as in Fig. 3(b). Except for the exclusion of lines originating in $10F$ levels, see Table V, the simulation shows excellent agreement with the observed spectrum.

The spectral features identified above with the intermediate coupling regime in the upper Rydberg level signal the onset of a transition to a new coupling regime that should characterize very highly excited Rydberg levels whose fine structure is much smaller than the core hyperfine structure. In this limit, the eigenstates would be characterized by

$$\vec{F}_c=\vec{J}_c+\vec{I}, \quad \vec{F}=\vec{F}_c+\vec{L}, \quad (13)$$

with the Rydberg electron's spin still negligible. The qualitative pattern of Rydberg fine structure would be completely changed, in this limit, by the influence of nuclear spin. For example, the $L=8$ Rydberg levels bound to the $J_c=2$ state of N^+ would no longer show a fivefold fine structure splitting in this limit, but would rather cluster in seven-, five-, and threefold fine-structure patterns around the free ion hyperfine levels. For ions with permanent quadrupole moments, such as N^+, the criterion for achieving this coupling limit may be approximated as

$$eQ\langle r^{-3}\rangle_{nL} \lesssim A_{\text{HFS}}. \tag{14}$$

Substituting the values of Q and A appropriate for the $J_c=2$ level of N^+ and the hydrogenic radial expectation value gives the condition

$$L \gtrsim \frac{300}{n} \tag{15}$$

for N Rydberg levels. This indicates, for example, that the majority of N Rydberg levels with $n \gtrsim 30$ should have this structure.

VI. RESULTS AND CONCLUSIONS

The spectrum of Fig. 3 contains experimental observations of excited states of N with $L>4$. Analysis of the spectrum indicates that to within the precision of the measurement, the positions of these levels are accounted for by an effective potential given in Eq. (2), and determines the best values of the parameters that occur in the potential. Using these estimates, the fine structure of a wide variety of other high-L Rydberg states of N may be predicted. In principle, the core parameters may also be calculated from the ionic wave function, and comparisons with the empirically determined values can serve as tests of *a priori* atomic structure calculations. This study also illustrates the subtle influence of core hyperfine interactions on Rydberg structure and demonstrates the onset of a transition to a new coupling regime expected to characterize most highly excited Rydberg atoms with hyperfine structure.

ACKNOWLEDGMENTS

[1] Edward S. Chang and Hajime Sakai, J. Phys. B **14**, L391 (1981). [We note that this reference uses a nonstandard definition of the atomic quadrupole moment that differs from the standard by a factor of $-(30)^{1/2}$ in the case of N^+.]

[2] James E. Bayfield, Rev. Sci. Instrum. **47**, 1450 (1976).

[3] S. L. Palfrey and S. R. Lundeen, Phys. Rev. Lett. **53**, 1141 (1984).

[4] W. G. Sturrus, P. E. Sobol, and S. R. Lundeen, Phys. Rev. Lett. **54**, 792 (1985).

[5] W. G. Sturrus, E. A. Hessels, P. W. Arcuni, and S. R. Lundeen, Phys. Rev. A **38**, 135 (1988).

[6] F. J. Deck, E. A. Hessels, and S. R. Lundeen, Phys. Rev. A **48**, 4400 (1993).

[7] R. F. Ward, Jr., W. G. Sturrus, and S. R. Lundeen, Phys. Rev.

A **53**, 113 (1996).

[8] R. F. Ward, Jr., Ph.D. thesis, University of Notre Dame, 1994 (unpublished).

[9] G. H. Shortley and B. Fried, Phys. Rev. **54**, 749 (1938).

[10] G. Racah, Phys. Rev. **61**, 537 (1942).

[11] A possible exception is the case of a core ion with hyperfine structure, discussed further in Sec. V of this paper.

[12] K. B. S. Eriksson, Ark. Fys. **19**, 229 (1961).

[13] P. Gronlund, Ark. Fys. **39**, 461 (1969).

[14] K. Bockasten, Phys. Rev. A **9**, 1087 (1974).

[15] This expression remains valid for slightly inelastic charge-transfer collisions if, as in this case, the internal energy transfer is the same for both projectile masses.

[16] A. Schirmacher and H. Winter, Phys. Rev. A **47**, 4891 (1993).